Fully coupled, dynamic model of a magnetostrictive amorphous ribbon and its validation

Bernhard Bergmair, Thomas Huber, Florian Bruckner, Christoph Vogler, Markus Fuger, and Dieter Suess

Articles you may be interested in

Fully coupled discrete energy-averaged model for Terfenol-D
J. Appl. Phys. 111, 054505 (2012); 10.1063/1.3687372

Experimental Evidence Violating Laws of Thermodynamics In Magnetostrictive Materials
AIP Conf. Proc. 1411, 158 (2011); 10.1063/1.3665237

Present status of theoretical modeling the magnetoelectric effect in magnetostrictive-piezoelectric
nanostructures. Part I: Low frequency and electromechanical resonance ranges
J. Appl. Phys. 107, 053904 (2010); 10.1063/1.3313919

A nonlinear constitutive model of magneto-thermo-mechanical coupling for giant magnetostrictive materials
J. Appl. Phys. 100, 063906 (2006); 10.1063/1.2338834

Hybrid transmission line-micromagnetic model for MR heads
J. Appl. Phys. 87, 5007 (2000); 10.1063/1.373230

Fully coupled, dynamic model of a magnetostrictive amorphous ribbon and its validation

Bernhard Bergmair,[1,2,a)] Thomas Huber,[1,2] Florian Bruckner,[2] Christoph Vogler,[2] Markus Fuger,[2] and Dieter Suess[2]

[1]*Institute of Analysis and Scientific Computing, Vienna University of Technology, Wiedner Hauptstr. 8, 1040 Vienna, Austria*
[2]*Institute of Solid State Physics, Vienna University of Technology, Wiedner Hauptstr. 8, 1040 Vienna, Austria*

Magnetostrictive amorphous ribbons are widely used in electronic article surveillance as well as for magnetoelastic sensors. Both applications utilize the fact that the ribbons' resonant frequency can be read out remotely by applying external magnetic AC fields. This paper proposes a magnetomechanical model to simulate the dynamics of such ribbons. The goal was to only use general material properties as input parameters, which are usually denoted in the data sheet of amorphous metals. Thus, only the magnetization curve at zero stress has to be gained via measurement. The magnetization under stress is calculated thereof. The equation of motion for a longitudinally oscillating ribbon is derived and coupled to Maxwell's equations for magnetostatics. The fully coupled initial value problem is solved simultaneously by a finite difference approach. The model is validated by comparing calculated and measured resonant frequencies of various amorphous ribbons, which turned out to be in good agreement. When slightly adapting single material properties from the data sheet, the match is almost perfect. The model is then used to calculate the local magnetic and mechanical properties inside static and vibrating ribbons. These local distributions can be directly linked to the field dependence of the resonant frequency and its higher harmonics. © 2014 AIP Publishing LLC. [http://dx.doi.org/10.1063/1.4861735]

I. INTRODUCTION

Amorphous magnetostrictive ribbons are used million-fold in Acousto-Magnetic (AM) systems for Electronic Article Surveillance (EAS).[1] They are also applied as magnetoelastic resonance sensors, which have gained increasing interest in recent years, as they provide an opportunity to remotely monitor a large variety of quantities.[2,3] Both applications utilize the fact that such a ribbon has a characteristic frequency, which can be read out remotely by applying magnetic AC fields and measuring the magnetic response signal. For most applications, this characteristic frequency is the resonant frequency of the ribbon's fundamental longitudinal oscillation mode. This resonant frequency is given by[4]

$$f_{\text{res}} = \frac{1}{2l} \sqrt{\frac{E}{\rho(1-\nu)}}, \tag{1}$$

where l is the length, E is Young's modulus, ν is the Poisson ratio, and ρ is the mass density of the ribbon. For a magnetostrictive material, Young's modulus depends on its magnetization, hence on its inner magnetic field (*Delta-E effect*). The field-dependent Young's modulus was described by Livingston for a linear magnetic material law[5] and more generally by Herzer[6]

$$\frac{1}{E(H)} = \frac{1}{E_{\text{s}}} + 9 \frac{\lambda_{\text{s}}^2 \mu_0}{J_{\text{s}}^2} \chi m^2, \tag{2}$$

where λ_{s} is the saturation magnetostriction, μ_0 is the vacuum permeability, J_{s} is the magnetic saturation polarization, χ is the differential susceptibility, and m is the normalized magnetization, i.e., the ratio of polarization J and J_{s}. H is the inner field. Both χ and m depend on the inner magnetic field, which is inhomogeneous, in general. Therefore, the simplistic Eq. (1) does not apply anymore for it assumes Young's modulus to be constant. The resonant frequency has to be calculated numerically. In addition, the magnetic properties of a magnetostrictive material are also stress dependent. Thus, to predict the dynamics of magnetostrictive ribbons, a fully coupled magneto-mechanical and stray field problem has to be solved.

Due to their versatile utilization for sensor and actuator applications, lots of work has been done on modeling the dynamics of magnetostrictive materials in recent years. Engdahl[7] solved the coupled magneto-mechanical problem of a magnetostrictive rod based on a 1D-finite differences method. To gain the necessary sample properties for the model, both magnetostriction and effective stiffness have to be measured as a function of applied magnetic field and stress. Magnetostatic interactions are not taken into account.

Baňas[8] used a micromagnetic approach with magnetostriction being incorporated as an additional magnetic field term in the Landau-Lifshitz equation. Magnetostatic interactions are not taken into account here either. The inner magnetic field is assumed to be known. The method is suitable for problem geometries on nanometer scale.

Peréz-Aparaicio and Sosa[9] formulated a fully coupled three-field problem, taking account of elastic, electric, and magnetic effects. Magnetostriction is represented via a set of linear constants which are functions of the stiffness at

a)Electronic mail: bernhard.bergmair@tuwien.ac.at

115, 023905-1

constant field, piezomagnetic coupling and permeability at constant stress. These material properties have to be characterized experimentally.

Cao *et al.*[10] modeled the dynamic hysteresis of a magnetostrictive actuator based on a modified Jiles-Atherton model including eddy currents. They used[12] model parameters which are found by a hybrid genetic algorithm by comparing the simulation results to the measured strain-field-hysteresis of the sample. Magnetostatic interactions are not taken into account. The inertial forces of the actuator-rod itself are neglected. Therefore, stress is only exerted at the rod's moveable end, which is constrained by a spring and an end mass.

Bottauscio *et al.*[11] modeled the dynamic behavior of a magnetostrictive actuator. The modeling of the magnetization hysteresis is based on an advanced Preisach model. The model parameters are gained from sets of static B-H-loops measured at different stresses. A finite element field analysis accounts for eddy currents in the magnetic materials. The actuator-rod is constrained by a spring on one side. As inertial forces are neglected again, the coupling between stress and magnetic quantities is only caused by the spring force increasing with the magnetostrictive elongation of the rod.

Evans and Dapino[12] developed a 3-D model for magnetostrictive transducers containing Maxwell's equations and structural dynamics. The model has been derived generally for nonlinear constitutive laws and was then implemented for a unimorph actuator with linear constitutive laws. Chakrabarti and Dapino[13] extended the approach into the nonlinear regime, using constitutive laws which are calculated by an energy-averaged model.[14]

Jin *et al.*[15] proposed a magneto-thermo-elastic coupled model to investigate the resonant frequency of an actuator. The nonlinear constitutive model is derived from a Taylor series expansion of Gibbs energy around the reference point with zero stress, zero magnetization, and a finite temperature. The nonlinear relation magnetization to magnetic field is modeled by the Langevin function. The magnetic and the elastic problems are solved iteratively until a certain convergence criterion is fulfilled.

In this paper, a model for describing the dynamics of a magnetostrictive amorphous ribbon is proposed. The goal was to predict the resonant frequency as a function of an externally applied field by only using general material properties. Fit parameters as well as extensive characterization measurements (like stress and field dependent magnetization) are avoided. The model is based on Livingston's work on the stress dependence of the magnetic properties of amorphous ribbons.[5] Livingston assumed an ideal magnetization behavior, where the magnetization component parallel to the external field linearly increases until it saturates with a sharp edge when reaching the anisotropy field. Real materials show a non-ideal, i.e., "rounded," transition from linear to saturated magnetization behavior in the vicinity of the anisotropy field. In this paper, a general method to calculate the stress induced transformation of these non-ideals, but still almost anhysteretic, hard axis magnetization curves is suggested. The one dimensional equation of motion for magnetostrictive materials is derived and simultaneously solved

together with Maxwell's equations for magnetostatics based on a finite difference approach. The stray field solution of Maxwell's equations also accounts for the ribbon's three dimensional shape. The calculated resonant frequencies at different magnetic fields are then compared to the resonant frequencies gained from experiments with ribbons of various material properties and shapes. Also detailed simulation results concerning static and dynamic local properties inside a ribbon—such as magnetization, strain, and Young's modulus—are presented as a function of the applied bias field.

The paper is structured as follows: In Sec. II, the model is derived. In Sec. II A, the scope of the model is described. In Sec. II B, the governing equations from literature concerning the ribbon's longitudinal oscillation and the coupling between mechanical and magnetic quantities are compiled. In Sec. II C, a method for calculating the stress-dependent magnetization from a measured magnetization curve at zero stress is developed. To account for the influence of an external magnetic field and for the ribbon's own stray field, a general solution of Maxwell's equations of magnetostatics is denoted in Sec. II D. The fully coupled system of equations is derived in Sec. II E, assuming the external field to be applied parallel to the ribbon's long axis and using a simplifying quasi-1D ansatz. In Sec. II F, these equations are discretized spatially, hence, forming a numerically solvable differential-algebraic system of equations. In Sec. III, the used third-party solver software is described. In Sec. IV, the calculated resonant frequencies of various ribbons are compared to the resonant frequencies obtained in according experiments. In Sec. V, the model is used to simulate local quantities and their dynamics in a vibrating magnetostrictive ribbon. In the appendix, a formulation of the Delta-E effect in the context of the one-dimensional equation of motion is derived. With this formulation, the ribbon's oscillation could be calculated analytically under the assumption of a homogeneous inner magnetic field in the ribbon and small strain amplitudes.

II. DERIVATION OF THE MODEL

A. Scope

The model describes the dynamic behavior of a magnetostrictive amorphous ribbon, which is subject to a time-variant external magnetic field. The external field is applied parallel to the ribbon's long axis (i.e., *x*-direction). Amorphous ribbons used for AM-EAS and magnetoelastic sensors (MES) are *transverse* or *oblique* annealed.[6] Both annealing processes induce a magnetocrystalline anisotropy with the easy axis being orthogonal to the ribbon's long axis. Figure 1 shows the emerging domain structure. If a magnetic field is applied in the *x*-direction, the magnetizations of the individual domains rotate towards the field vector. The resulting macroscopic net-magnetization is parallel to the *x*-direction, as the *y*- and *z*-components of neighboring domains cancel each other out (Fig. 2).

Ribbons used for EAS and MES usually have a slender shape. To model their dynamic behavior, it is therefore sufficient to create a one-dimensional finite difference grid by partitioning the ribbon lengthwise into a finite number of
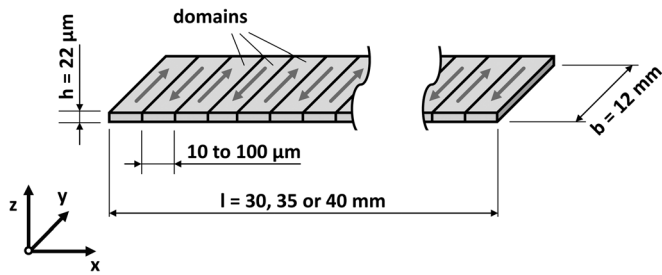
FIG. 1. Schematic domain structure of an amorphous ribbon with easy axis in *y*-direction.

numerical elements (Fig. 3). Hence, only spatial variations in *x*-direction are taken into account, whereas in the (*y*, *z*)-cross section, all considered quantities are assumed to be constant.

B. Magnetomechanical coupling

In a magnetostrictive material, mechanical and elastic quantities are coupled. The strain ε and the magnetic polarization J depend on both the mechanical (tensile) stress σ and the magnetic field H (see, for instance, Engdahl[16])

$$\begin{aligned} \varepsilon &= \varepsilon(\sigma, H), \\ J &= J(\sigma, H). \end{aligned} \quad (3)$$

The equation of motion in one dimension without damping is

$$\rho \frac{\partial^2}{\partial t^2} u(x, t) = \frac{\partial}{\partial x} \sigma(x, t), \quad (4)$$

where $u(x, t)$ is the longitudinal displacement of an element at the original position x, ρ is the mass density, and σ is the tensile stress in *x*-direction. In a magnetostrictive material, the total strain is the sum of an elastic component ε^{e} and the magnetostrictive strain ε^{m}

$$\varepsilon = \varepsilon^{\mathrm{e}} + \varepsilon^{\mathrm{m}}. \quad (5)$$

Only the elastic strain contributes to Hooke's law

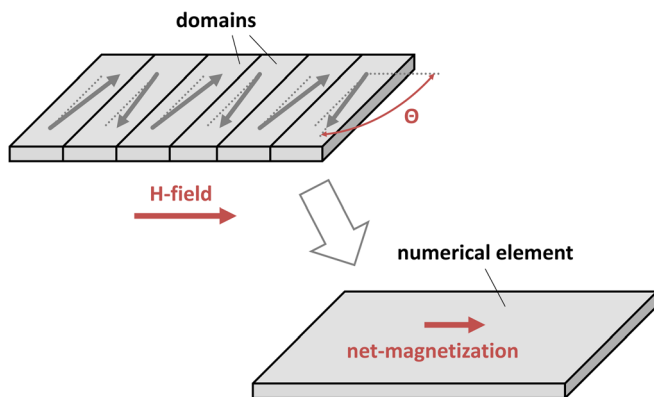$$\sigma = E_{\mathrm{s}} \varepsilon^{\mathrm{e}}, \quad (6)$$

FIG. 2. Rotational magnetization process in an external field. One numerical element contains several domains. The net-magnetization is parallel to the *x*-axis.
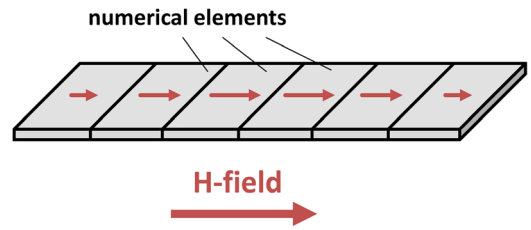

FIG. 3. One-dimensional grid for the finite difference method. The arrows symbolize the net-magnetization in each element.

where E_{s} is Young's modulus, which can be measured for magnetostrictive materials under magnetic saturation. The total strain ε is given by the displacement u

$$\varepsilon(x, t) = \frac{\partial}{\partial x} u(x, t). \quad (7)$$

For a ferromagnetic material, the magnetic strain of an ensemble of grains can be calculated from the average direction of the grain magnetizations[17]

$$\varepsilon^{\mathrm{m}} = \frac{3\lambda_{\mathrm{s}}}{2} \left(\langle \cos(\theta)^2 \rangle - \frac{1}{3} \right), \quad (8)$$

where θ denotes the angle of the local grain magnetization with respect to the direction in which the magnetostriction is measured. The term $-\frac{1}{3}$ implies that a material with randomly oriented spins has zero magnetostriction. In the case of a uniform hard-axis magnetization $\cos(\theta)$ is constant for all grains in the ensemble. Thus, one can claim

$$\langle \cos(\theta)^2 \rangle = \langle \cos(\theta) \rangle^2 = \left(\frac{J_x}{J_{\mathrm{s}}} \right)^2 =: m^2 \quad (9)$$

with the magnetic polarization in *x*-direction J_x, the saturation polarization J_{s}, and the normalized magnetization m. Inserting (5), (7), (8), and (9) in (6) yields

$$\sigma = E_{\mathrm{s}} \left(\frac{\partial u}{\partial x} - \frac{3\lambda_{\mathrm{s}}}{2} \left(m^2(H, \sigma) - \frac{1}{3} \right) \right). \quad (10)$$

It should be noted that this is not an explicit expression for σ as the normalized magnetization m of a magnetostrictive material still depends on σ. The inner magnetic field H is unknown, too as it depends on the shape of the demagnetizing field produced by the ribbon. Moreover, the function $m(H, \sigma)$ is yet to be defined.

C. Transformation of the magnetization under stress

Considering the ideal case of an anhysteretic linear material law, which sharply saturates at the stress dependent anisotropy field $H_{A\sigma}$, the normalized magnetization under stress can be calculated by[5]

$$m(H, \sigma) = \begin{cases} \dfrac{H}{H_{A\sigma}}, & 0 < H < H_{A\sigma}, \\ 1, & H_{A\sigma} \le H \end{cases} \quad (11)$$

where

$$H_{\mathrm{A}} := \frac{2K_{\mathrm{u}}}{J_{\mathrm{s}}}, \qquad (12)$$

$$\sigma_{\mathrm{c}} := \frac{2K_{\mathrm{u}}}{3\lambda_{\mathrm{s}}}, \qquad (13)$$

$$H_{\mathrm{A}\sigma} := \frac{2K_{\mathrm{u}} - 3\lambda_{\mathrm{s}}\sigma}{J_{\mathrm{s}}} = \left(1 - \frac{\sigma}{\sigma_{\mathrm{c}}}\right)H_{\mathrm{A}}, \qquad (14)$$

with the anisotropy constant K_{u}, the saturation magnetostriction λ_{s}, and the saturation polarization J_{s}. Figure 4 shows the normalized magnetization as a function of the normalized magnetic field at different tensile and compressive stresses. To better express the stress dependencies in (11), a field H_{t} which is scaled by a stress dependent factor can be defined

$$H_{\mathrm{t}} := \left(1 - \frac{\sigma}{\sigma_{\mathrm{c}}}\right)^{-1} H. \qquad (15)$$

Substituting $H_{\mathrm{A}\sigma}$ and H by (14) and (15) in (11) yields

$$m(H,\sigma) = \begin{cases} \dfrac{H_{\mathrm{t}}}{H_{\mathrm{A}}}, & 0 < H_{\mathrm{t}} < H_{\mathrm{A}} \\ 1, & H_{\mathrm{A}} \le H_{\mathrm{t}} \end{cases}. \qquad (16)$$

This is equivalent to a magnetization curve with the *zero stress* anisotropy field H_{A} evaluated at a field H_{t}. Thus, the whole stress-dependence of the ideal magnetization function can be reduced to the following *stress-transformation*:

$$m(H,\sigma) = m(H_{\mathrm{t}}, 0) =: m_0(H_{\mathrm{t}}), \qquad (17)$$

where $m_0(H)$ is the magnetization curve at zero stress. Hence, magnetization curves at finite stresses $\sigma < \sigma_{\mathrm{c}}$ can be calculated there from by just scaling the H-axis. It should be noted that this stress-transformation depends on the anisotropy constant, hence on the anisotropy field.

Amorphous specially annealed materials show a close-to-ideal hard-axis magnetization curve (Fig. 5). The observed rounded shape can be explained by an underlying anisotropy field distribution[18] in contrary to the singular anisotropy field of a sharply edged ideal magnetization curve. Thus, the stress-transformation above cannot be generally applied in a straight forward manner, as a unique anisotropy field does not exist. First, the observed rounded magnetization curve at zero stress has to be decomposed into its components. Each of these components is represented by a sharply edged magnetization curve with a unique anisotropy energy. Second, every component has to be stress-transformed on its own, using this particular anisotropy energy. Third, the transformed sharply edged magnetization curves can be recomposed to obtain the real (rounded) magnetization curve under stress. Yet, for narrow anisotropy distributions, the stress-transformation can be applied straight forward to the observed magnetization curve by using an effective anisotropy constant $K_{\mathrm{u,eff}}$ instead of taking the whole distribution into account. This paper is based on the latter approach. Moreover, the measured magnetization curve under zero stress $m_0(H)$ is simplified as anhysteretic spline-function. This zero stress spline function is then taken as input for the simulation from which all values under stress $m(H,\sigma)$ are calculated using (17).

D. Magnetostatic problem

The inner magnetic field $\boldsymbol{H}$ is the sum of the applied external field $\boldsymbol{H}_{\mathrm{ext}}$ and the stray field $\boldsymbol{H}_S$ of the magnetized ribbon

$$\boldsymbol{H} = \boldsymbol{H}_{\mathrm{ext}} + \boldsymbol{H}_S. \qquad (18)$$

Eddy currents are neglected, as amorphous metals have a relative high electrical resistivity and the resonant frequencies of the used ribbons are in the kHz-regime. At these frequencies, also the magnetization dynamics of the current rotational magnetization processes can be neglected. Maxwell's equations therefore read

$$\nabla \cdot \boldsymbol{B} = 0, \qquad (19)$$

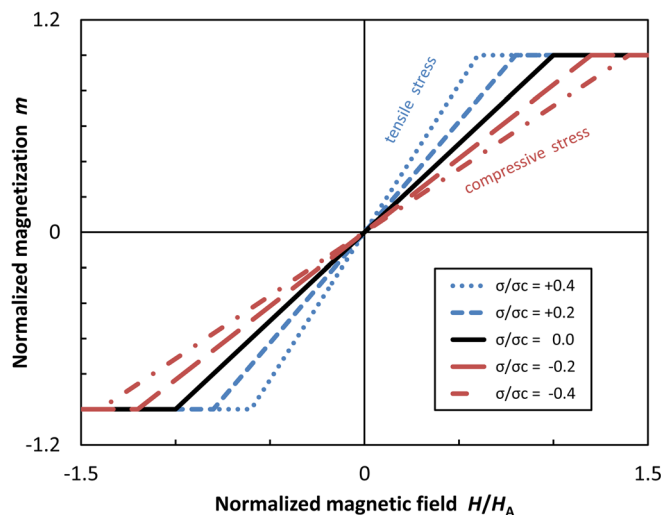$$\nabla \times \boldsymbol{H} = 0, \qquad (20)$$

FIG. 4. Ideal magnetization curves at different stresses of a material with positive magnetostriction. Stress, magnetic field, and magnetization are parallel. The influence of the stress is equivalent to a scaling of the magnetic field axis.
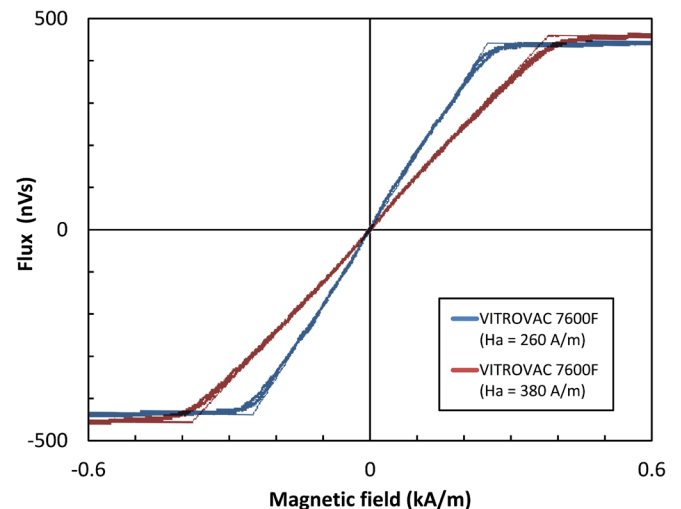

FIG. 5. Hard-axis magnetization of the amorphous metal VITROVAC 7600 F for two different anisotropy fields.

where

$$\boldsymbol{B} = \mu_0 \boldsymbol{H} + \boldsymbol{J}. \qquad (21)$$

The solution is[19]

$$\boldsymbol{H} = \boldsymbol{H}_{\text{ext}} - \frac{1}{4\pi} \nabla \left(\int_V \frac{\rho_{\text{m}}(\boldsymbol{r}')}{|\boldsymbol{r} - \boldsymbol{r}'|} \mathrm{d}V' + \oint_{\partial V} \frac{\sigma_{\text{m}}(\boldsymbol{r}')}{|\boldsymbol{r} - \boldsymbol{r}'|} \mathrm{d}S' \right) \qquad (22)$$

with the magnetic volume charge density

$$\rho_{\text{m}} = -\nabla \cdot \boldsymbol{J}/\mu_0 \qquad (23)$$

and the magnetic surface charge density

$$\sigma_{\text{m}} = \boldsymbol{n} \cdot \boldsymbol{J}/\mu_0, \qquad (24)$$

where V denotes the volume of the ribbon and $\boldsymbol{n}$ denotes the surface normal at the boundary of V. Hence, (22) depends on the magnetic polarization $\boldsymbol{J}$ and on the normalized magnetization $\boldsymbol{m}$, respectively. Equations (4), (10), and (22) have to be solved simultaneously.

E. Fully coupled problem

For the derivation of the numerical model, the aforementioned assumptions are taken into account in this section: i.e., all quantities are assumed to be constant in the (y, z)-cross sections. The external field is applied parallel to the x-axis. Thus, the macroscopic magnetization is also parallel to the x-direction. With these assumptions, it is not possible to satisfy both Maxwell's equations and the material law at every point of the ribbon. It is therefore only demanded that they are fulfilled on the ribbon's long axis ($y = z = 0$). This yields a *quasi-one-dimensional* model. It should be pointed out that (inside the framework of the above mentioned assumptions), the stray field is nonetheless calculated on a three-dimensional basis.

For symmetry reasons, only the x-component of the magnetic field vector is nonzero on the ribbon's long axis. With

$$\boldsymbol{H}_{\text{ext}} := H_{\text{ext}} \hat{e}_x, \qquad (25a)$$

$$\Rightarrow \boldsymbol{H}(x, y = 0, z = 0) = H(x)\hat{e}_x, \qquad (25b)$$

where $\hat{e}_x$ is the unit vector in x-direction, the x-component of the vector Eq. (22) along the ribbon's long axis reads

$$H(x) = H_{\text{ext}} - \frac{1}{4\pi} \frac{\partial}{\partial x} \left(\int_V \frac{\rho_{\text{m}}(\boldsymbol{r}')}{|x\hat{e}_x - \boldsymbol{r}'|} \mathrm{d}V' + \oint_{\partial V} \frac{\sigma_{\text{m}}(\boldsymbol{r}')}{|x\hat{e}_x - \boldsymbol{r}'|} \mathrm{d}S' \right), \qquad (26a)$$

$$= H_{\text{ext}} - \frac{1}{4\pi\mu_0} \int_V \frac{\partial J_x(\boldsymbol{r}')}{\partial x'} \frac{(x - x')}{\left[(x - x')^2 + y'^2 + z'^2\right]^{\frac{3}{2}}} \mathrm{d}V'$$

$$+ \frac{1}{4\pi\mu_0} \oint_{\partial V} \boldsymbol{n}(\boldsymbol{r}') \cdot \hat{e}_x J_x(\boldsymbol{r}') \frac{(x - x')}{\left[(x - x')^2 + y'^2 + z'^2\right]^{\frac{3}{2}}} \mathrm{d}S'. \qquad (26b)$$

For the subsequent numerical treatment, it is helpful to substitute the second time derivative of u in (4) by introducing the velocity v

$$v(x, t) := \frac{\partial}{\partial t} u(x, t). \qquad (27)$$

And last, the ribbon's cuboid-shape of the size $l \times b \times h$ in x-, y-, and z-directions is considered. The total system of equations then reads

$$0 = \frac{\partial}{\partial t} u - v, \qquad (28a)$$

$$0 = \rho \frac{\partial}{\partial t} v - \frac{\partial}{\partial x} \sigma, \qquad (28b)$$

$$0 = \frac{\sigma}{\lambda_s E_s} - \frac{1}{\lambda_s} \frac{\partial u}{\partial x} + \frac{3}{2} m(H, \sigma)^2 - \frac{1}{2}, \qquad (28c)$$

$$0 = H - H_{\text{ext}} + \frac{J_s}{4\pi\mu_0} \int_{x'} \frac{\partial m(H^{x'}, \sigma^{x'})}{\partial x'} C^{x-x'} \mathrm{d}x'$$
$$- \frac{J_s}{4\pi\mu_0} \sum_{x' = \pm \frac{l}{2}} \text{sgn}(x') m^{x'}(H, \sigma) C^{x-x'}, \qquad (28d)$$

where the spatial dependence of the quantities in the x'-integral is clarified by superscripts. For the integrals over the cross section, the abbreviation

$$C^{x-x'} = \int_{y'=-\frac{b}{2}}^{\frac{b}{2}} \int_{z'=-\frac{h}{2}}^{\frac{h}{2}} \frac{x - x'}{\left[(x - x')^2 + y'^2 + z'^2\right]^{\frac{3}{2}}} \mathrm{d}y' \mathrm{d}z' \qquad (29)$$

has been used. They can be calculated analytically with a rather long expression (see Akoun and Yonnet,[20] Appendix 1 or Engel-Herbert and Hesjedal[21]). The unknown quantities in this system of equations are u, v, σ, and H. All of them are functions of the position along the x-axis and time.

F. Spatial discretization

To solve this problem numerically, the geometry has to be spatially discretized in the x-dimension. Due to the cuboidal shape of the ribbon, a finite difference approach was chosen. Hence, the ribbon is partitioned into a chain of n homogeneous cuboids (i.e., numerical elements, see Fig. 3). Each of them has the length q. The advantage of the finite difference approach is that the stray field of the resulting cuboidal numerical elements can be calculated by employing the analytical expression for Eq. (29). As a consequence of the emerging difference quotients, the quantities u, v, h, and $\partial\sigma/\partial x$ are defined at the n centers of the elements, denoted by integer superscripts. Whereas the quantities σ and $\partial u/\partial x$ are defined at the $n-1$ interfaces between the elements and at the borders at $x = \pm\frac{l}{2}$, denoted by the half-integer superscripts. The partial derivatives are replaced by the corresponding finite difference quotients

$$\left(\frac{\partial \sigma}{\partial x}\right)^i \to \frac{\sigma^{i+\frac{1}{2}} - \sigma^{i-\frac{1}{2}}}{q}, \tag{30a}$$

$$\left(\frac{\partial u}{\partial x}\right)^{i+\frac{1}{2}} \to \frac{u^{i+1} - u^i}{q}. \tag{30b}$$

As the single cuboids have a homogenous magnetization, the integral over x' in (28d) vanishes. Instead the term for the surface charges has to take into account the surfaces of all the cuboids. Hence, an additional sum appears. It should be noted that the additional sum also includes the case $i = j$, hence taking into account the demagnetizing field of the respective numerical element itself. For every numerical element $i \in \{1, 2, ..., n\}$, the discretized form of the system of Eq. (28) has to be fulfilled

$$0 = \dot{u}^i - v^i, \tag{31a}$$

$$0 = \rho \dot{v}^i - \frac{\sigma^{i+\frac{1}{2}} - \sigma^{i-\frac{1}{2}}}{q}, \tag{31b}$$

$$0 = \frac{\sigma^{i+\frac{1}{2}}}{\lambda_s E_s} - \frac{1}{\lambda_s} \frac{u^{i+1} - u^i}{q}$$
$$+ \frac{3}{2} m \left(\frac{H^i + H^{i+1}}{2}, \sigma^{i+\frac{1}{2}}\right)^2 - \frac{1}{2}, \tag{31c}$$

$$0 = H^i - H^i_{\text{ext}} - \frac{J_s}{4\pi\mu_0}$$
$$\times \sum_{j=1}^{n} \sum_{\Delta j = \pm \frac{1}{2}} \text{sgn}(\Delta j)\, m\left(H^j, \frac{\sigma^{j-\frac{1}{2}} + \sigma^{j+\frac{1}{2}}}{2}\right) C^{x^i - x^{j+\Delta j}}. \tag{31d}$$

The unknown quantities in this system of equations are $u^i, v^i, \sigma^{i+\frac{1}{2}}$ and H^i for all n or $n+1$ values of the index i. They can be wrapped up to a single vector with $4n$ dimensions

$$y(t) = \begin{pmatrix} u(t) \\ v(t) \\ \sigma(t) \\ H(t) \end{pmatrix}. \tag{32}$$

This vector of unknowns is now only a function of time. The set of Eq. (31) is a differential-algebraic equation (DAE) system. It can be expressed as a vector function, which also has $4n$ dimensions

$$0 = F(t, y(t), \dot{y}(t)), \tag{33}$$

where the explicit time dependence can, for example, be caused by a time varying external magnetic field.

III. SOFTWARE

The initial value problem for (33) was solved with Sundials IDA package.[22] Starting, for instance, from trivial initial conditions, IDA conducts the time evolution. Therefore, the time is discretized into a succession of variable time steps h_m. For each discrete time step m, IDA uses Backward Differentiation Formulas (BDFs) to substitute the unknown time derivatives $\dot{y}_m$ by a linear function of known y_{m-k} from former time steps and the unknown y_m from the present time step

$$\dot{y}_m = \frac{1}{h_m} \sum_{k=0}^{p} (\alpha_k)_m\, y_{m-k}. \tag{34}$$

The order p and the coefficients α_k are variably managed by IDA itself. IDA also chooses the time step h_m by using a set of local error estimates. Hence, the differential-algebraic system (33) is replaced by a nonlinear algebraic system

$$0 = G_m(t_m, y_m), \tag{35}$$

which is solved at every time step by a Newton iteration. For each step of the Newton iteration, a linear system of equations needs to be solved, which is done by means of a matrix-free Generalized Minimal Residual (GEMRES) Krylov method. Arising Jacobian vector products are replaced by finite difference approximations.

IV. MODEL VERIFICATION

To validate the derived model, the free longitudinal vibration of various magnetostrictive ribbons have been both measured and simulated. The fundamental resonant frequency has then been determined as a function of the applied homogeneous external magnetic bias field. In both cases, the vibration has been induced by applying an additional time-dependent magnetic field (excitation field). After turning off the excitation field, the ribbon vibrates freely at its resonant frequency. The resonant frequency has been determined by conducting a Fast Fourier Transform (FFT) of the measured or simulated time series of the ribbon's magnetization.

The ribbons have been made of the amorphous metal VITROVAC [Ref. 23] 7600 F with ($H_{\text{A,eff}} = 260\,\text{A/m}$) and ($H_{\text{A,eff}} = 380\,\text{A/m}$) from Vacuumschmelze. The ribbons have been cut into lengths of 30, 35, and 40 mm. For the simulation, a ribbon has been mathematically divided into 80 numerical elements in the framework of the finite difference algorithm. Table I lists all of the sample properties, which are used as model input. Most of the parameters are taken from the material data sheet. The spline function for the magnetization curve at zero stress is derived from Fig. 5 and applies to both materials

$$m_0(H) = \begin{cases} \dfrac{H}{H_A}, & 0 \le H < 0.8\,H_A, \\[2mm] \text{cubic polynomial}, & 0.8\,H_A \le H \le 1.25\,H_A, \\[2mm] 1, & 1.25\,H_A \le H. \end{cases} \tag{36}$$

The only fit-parameter is Young's modulus. It was adapted in order to make the simulated resonant frequency at $H_{\text{ext}} = 0$ matches the measured frequency. This fitted Young's modulus already includes Poisson's ratio. The Poisson ratio takes into

TABLE I. Model input parameter.

Parameter	Symbol	Magnitude	Source
Anisotropy field (effective)	$H_{A,\mathrm{eff}}$	260 or 380 A/m	data sheet
Saturation polarization	J_s	1.74 T	data sheet
Saturation magnetostriction	λ_s	42 ppm	data sheet
Mass density	ρ	7480 kg/m^3	data sheet
Normalized hard axis magnetization	$m(H, \sigma = 0)$	cubic spline	data sheet
Young's modulus	E_s	159.76 GPa	fitted
Ribbon length	l	30, 35, or 40 mm	measured
Ribbon width	b	12.3 mm	measured
Ribbon thickness	h	22 μm	calculated

account that the longitudinal oscillation yields transverse deformations at the same time.[4]

Figure 6 shows the used experiment setup. The magnetostrictive ribbon was placed on a plane surface in the center of the coils. A homogeneous constant bias field in parallel to the x-axis was generated by the bias coil. The strength of the generated bias field per coil current was measured in the center of the coil using the gauss meter *Bell 610*. The excitation coil produced an exponentially decaying sinusoidal field in the same direction. After turning off this excitation field, the ribbon continued to vibrate longitudinally for about one millisecond in its self oscillation modes. The pickup coil catched the ribbon's stray field, which was produced by its oscillating magnetization. A fast Fourier transform was then performed on the signal. The resonant frequency was defined as the position of the spectral peak maximum. Both controlling the experimental setup and analyzing the signal was done by a emphNational Instrument LabView program.

The results are plotted in Fig. 7. With the denoted parameters, the simulated resonant frequencies are in good agreement with the measured ones. However, they match better for long hard magnetic ribbons than for short soft magnetic ribbons. The intrinsic approximations of the presented model are a possible reason. The quasi-one-dimensional nature of the model is better suited for long ribbons. For shorter ribbons, the assumption of uniform quantities throughout the cross section becomes inapplicable at some point. Another possible explanation for the discrepancies between experiment and simulation are imprecisions of the used material
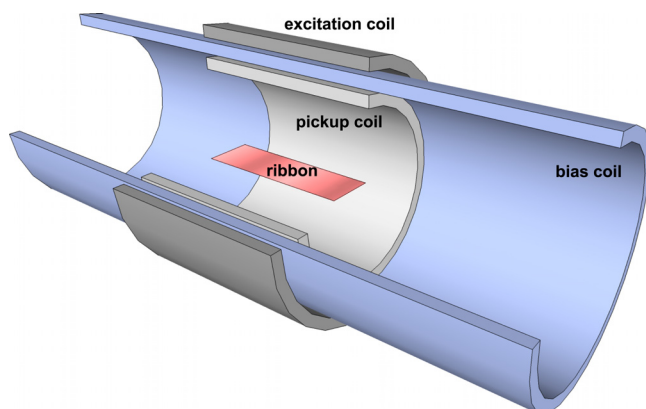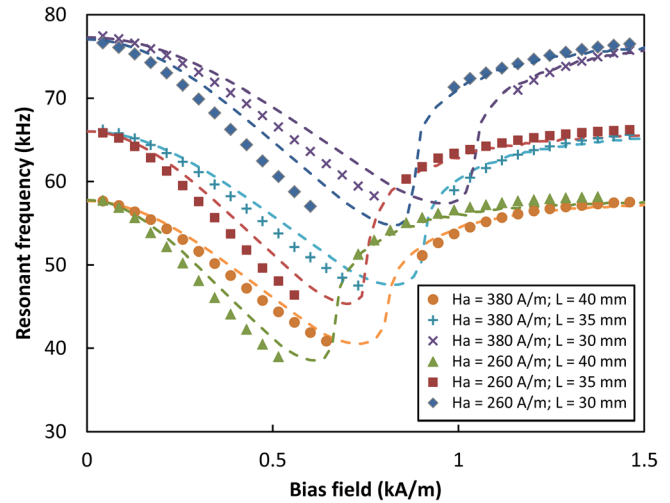

FIG. 6. Experimental setup.

FIG. 7. Comparison of measured (symbols) and simulated (dashed lines) resonant frequencies of various amorphous ribbons. For the simulation, the parameters from Table I have been used.

parameters. The latter reason is likely to have some influences anyway, as the material parameters denoted in the data sheet are only mean values of the whole batch.

All of them can differ from the actual properties of the used samples. When, for instance, a saturation magnetization J_s lowered by 8% is used for the simulation, the result almost exactly matches the measured frequencies (see Fig. 8). Increasing the saturation magnetostriction λ_s by 12% leads to very similar improvements (not plotted). The lack of experimental data in the vicinity of the frequency minima is due to the very weak signal strength at these bias fields.

V. SIMULATION RESULTS

With the presented model, it is possible to gain insights into the physical phenomena that are responsible for the resonant frequency behavior as a function of bias field. This section shows the spatial distributions of some fundamental
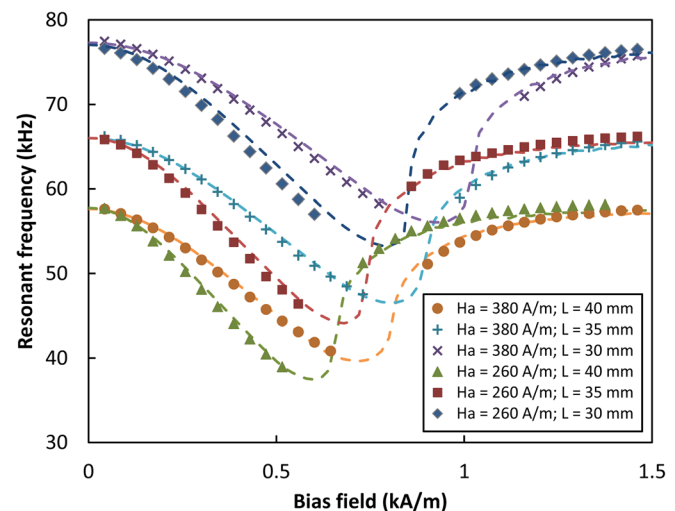

FIG. 8. Comparison of measured (symbols) and simulated (dashed lines) resonant frequencies of various amorphous ribbons. For the simulation, the parameters from Table I have been used, with the exception of J_s, which was fitted from the original 1.74 T to 1.60 T.

quantities of the coupled magnetoelastic system of a magnetostrictive ribbon and their dynamics during the ribbon's oscillation.

These quantities are the governing response functions, which can be deduced from Eq. (3): the material laws with a field dependent Young's modulus E_H and the strain dependent differential susceptibility χ_σ

$$\frac{\partial \varepsilon}{\partial \sigma}\bigg|_H =: \frac{1}{E_H(\sigma, H)},$$
$$\frac{\partial J}{\partial H}\bigg|_\sigma =: \mu_0\, \chi_\sigma(\sigma, H), \tag{37}$$

and the magnetomechanical coupling coefficient d derived from Maxwell's rule

$$\frac{\partial \varepsilon}{\partial H}\bigg|_\sigma \equiv \frac{\partial J}{\partial \sigma}\bigg|_H =: d(\sigma, H). \tag{38}$$

The latter, for instance, describes how easily a mechanical oscillation of the ribbon can be caused by magnetic AC fields and, vice versa, also describes the amplitude of the oscillating magnetic moment caused by such a mechanical oscillation. All these quantities are scalars representing the components along the x-axis.

A. Numerical experiment

To obtain these quantities, the following numerical experiment was conducted.

While over critically damping the system by an artificial damping constant, the bias field in x-direction was slowly turned on. Hence, the ribbon elongates as it is not constrained in any way. When the system reached its idle state, the local distributions of the quantities of interest were extracted to characterize the static conditions in the biased ribbon.

To gain insights into the dynamics of the oscillating ribbon, a similar simulation was repeated. But this time, an additional DC excitation field of 1 A/m parallel to the bias field was turned on together with the bias field. Then, the damping was switched off. Subsequently, the excitation field was turned off within 10 μs in the form the descending half of a cosine period. This falling edge in the total applied field excites oscillations of the ribbon.

With the bias field staying turned on, the local oscillation amplitudes of the respective quantities were determined. They are defined as half difference between the occurring maximum and minimum values in the time series. The frequency spectrum of the oscillation at a certain bias field was obtained by an FFT of a 2.5 ms long time series of the oscillating length of the ribbon. For the FFT, a Hanning window was used. It should be noted that the resulting amplitudes and spectra depend on the form and strength of the excitation field. However, the principle patterns and fundamental frequencies are widely independent from the excitation field.

B. Results

The spatial distribution inside the *static* ribbon and its dependence on the external bias field is plotted in Fig. 9. In
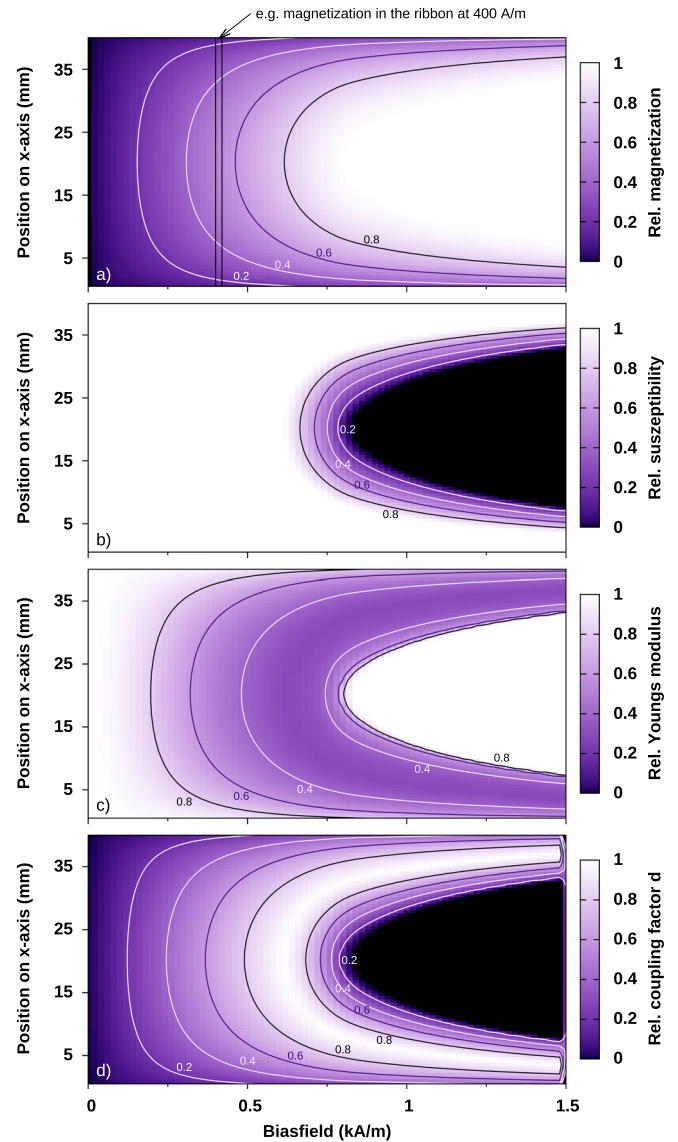

FIG. 9. Simulated spatial distribution of various quantities inside a static magnetostrictive ribbon as a function of the applied external bias field (horizontal axis). The position along the x-axis of the ribbon is represented by the vertical axis of each frame. For the simulation, the parameters from Table I with l = 40 mm and H_a = 380 A/m have been used. (a) Relative magnetization J/J_s, (b) relative magnetic susceptibility χ_σ/χ_i with χ_i = 3644, (c) relative Young's modulus (Delta-E effect) E_H/E_s, (d) magnetomechanical coupling coefficient d.

these 2D-plots, each vertical line of pixels represents the spatial distribution of the respective quantity along the ribbon's long axis at a certain strength of the applied bias field.

The magnetization is plotted in Fig. 9(a). Despite the homogeneous external bias field, the magnetization inside the ribbon always has a distinct maximum at the center. This is due to the ribbon's demagnetizing stray field, which is strongest at the two edge regions. The overall pattern is determined by two regimes: For lower bias fields, the susceptibility (Fig. 9(b)) is constant and the magnetization is proportional to the inner magnetic field (i.e., the superposition of bias field and stray field). For bias fields above 750 A/m, the magnetization of the center region starts to saturate, the susceptibility becomes zero. In Fig. 9(c), the Delta-E effect is plotted. The values were calculated according to Eq. (2)

using the simulated local quantities of the susceptibility and magnetization. The softening of the magnetostrictive ribbon (lowering of its effective Young's modulus) reaches its maximum for highly magnetized but not yet saturated areas. The dependence of the resonant frequency on the applied field (compare Fig. 7) is largely determined by the softening of the ribbon's center region. The influence of Young's modulus in the ribbon's off-centered areas can be seen from the fact that even when Young's modulus in the ribbon's center is saturated, its resonant frequency is not. The coupling coefficient (Fig. 9(d)) follows a similar pattern like the Delta-E effect: There is no first order magnetostrictive effect for small magnetizations (see Eq. (8)), nor do small changes of

mechanical quantities have any influence on the magnetization of magnetically saturated regions.

The spatial distribution of the oscillation amplitudes of strain, magnetization, and stress inside a *vibrating* ribbon is plotted in Figs. 10(a)–10(c). Both strain (a) and magnetization (b) oscillate around their respective profiles of the idle state, which are given by the afore described bias magnetization (see Fig. 9(a)) and the according magnetostrictive strain. The stress (c) oscillates around zero, as the ribbon is not constrained on any side. All three amplitudes show a similar profile. The oscillation is zero at zero bias field as there does not exist any magnetomechanical coupling. With an increasing bias field, the plotted amplitudes are approximately proportional to the static magnetomechanical coupling constant in the center region of the ribbon (compare Fig. 9(d)). Therefore, the oscillation immediately nearly ceases when the magnetization starts to saturate there.

The Fourier spectra of the oscillating total length of the ribbon are plotted in Fig. 10(d). The vertical axis represents the frequency domain at a certain bias field. When the center region is magnetically saturated the maximum oscillation amplitudes no longer occur in the center but in the upper and lower thirds of the ribbon. Hence, the higher harmonics gain more weight at these bias fields. The fundamental oscillation mode reaches its maximum amplitude at a bias field of 700 A/m with a frequency of 40.6 kHz. The maximum amplitude of the third harmonic is only 0.2% of the maximum fundamental amplitude. It occurs at a bias field of 860 A/m with a frequency of 157.8 kHz. And the peak amplitude of the fifth harmonic is only 0.04% of the maximum fundamental amplitude. It occurs at a bias field of 1300 A/m with a frequency of 277.5 kHz.

VI. CONCLUSION

In summary, we deduced a numerical model, which describes the longitudinal vibration dynamics of magnetostrictive ribbons. The model is valid for anhysteretic hard-axis magnetization processes induced by an external time-dependent magnetic field. It accounts for magnetostatic coupling and non-linear relations of the magnetization to strain and the magnetic field. The model was tested by both measuring and simulating the field-dependent resonant frequencies of six sample ribbons with different lengths and anisotropy fields. It was shown that the model reproduces the qualitative behavior very well and also yields fair agreement of the absolute values of the resonant frequencies as a function of the external field. At this only, the unknown Young's modulus of the used material was fitted. If input parameters like the saturation magnetization are slightly adapted, the simulation results match the measured frequencies even almost exactly. It should be stressed out that only two fit parameters are used to reproduce the whole frequency-field-dependence of all of the different sample ribbons. Finally, the simulated static local quantities of the magnetically biased ribbon were presented and linked to the field dependence of the resonant frequency. Also the simulated local amplitudes during the oscillation
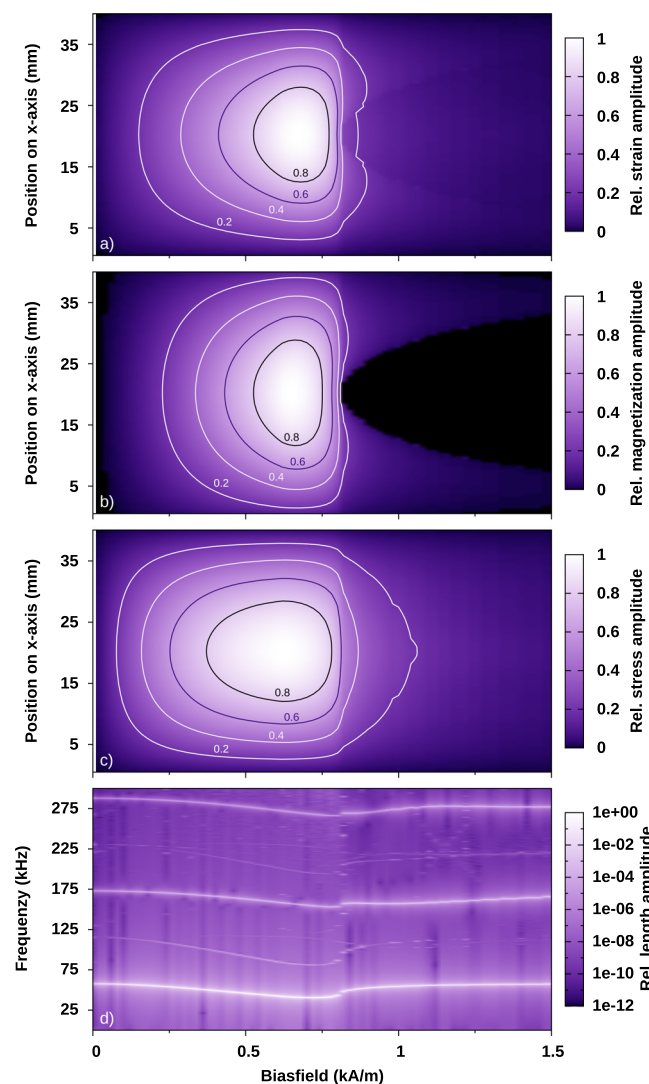

FIG. 10. Simulated spatial distribution of the oscillation amplitudes of various quantities inside a longitudinally vibrating magnetostrictive ribbon as a function of the applied external bias field (horizontal axis). The oscillation was excited by a falling edge in the applied field of 1 A/m within 10 μs. The falling edge had the form of half a period of a cosine. The position along the x-axis of the ribbon is represented by the vertical axis of each frame. For the simulation, the parameters from Table I with $l = 40$ mm and $H_a = 380$ A/m have been used. (a) Relative amplitude of the strain ε, where 1 corresponds to 4.86 nm, (b) relative amplitude of the magnetic polarization J, where 1 corresponds to 0.99 mT, (c) relative amplitude of the stress σ, where 1 corresponds to 9.66 kPa, (d) Fourier spectra of the oscillation of the ribbon length, where the vertical axis represents the frequency domain (arbitrary units).

and their connection to higher harmonics in the frequency spectra were discussed.

ACKNOWLEDGMENTS

APPENDIX: ANALYTICALLY SOLVABLE LIMITING CASE: HOMOGENEOUS INNER MAGNETIC FIELD AND SMALL STRAIN AMPLITUDES

Assuming a homogeneous inner magnetic field H and small stress amplitudes, the equation of motion (4) with (10) can be simplified. From the simplified form, an expression for the Delta-E effect can be found. Therefore, an explicit expression for σ has to be obtained from (10). This can be done by approximating the term $m^2(H, \sigma)$ by a Taylor expansion in σ at $\sigma = \sigma_0$ to the first order.

$$
\begin{aligned}
m^2(H, \sigma) &= m_0^{\,2}(H_t(\sigma)), \\
&\approx m_0^{\,2}\big|_{H_t(\sigma_0)} + \frac{\partial(m_0^{\,2})}{\partial\sigma}\bigg|_{H_t(\sigma_0)} (\sigma - \sigma_0), \\
&= m_0^{\,2} + 2\,m_0\big|_{H_t(\sigma_0)} \frac{\partial m_0}{\partial H_t}\bigg|_{H_t(\sigma_0)} \frac{\partial H_t}{\partial\sigma}\bigg|_{\sigma_0} (\sigma - \sigma_0), \\
&= m_0^{\,2}\big|_{H_t(\sigma_0)} + 2\,\frac{\mu_0}{J_s}(\chi\, m_0)\big|_{H_t(\sigma_0)} \\
&\quad \times \left(1 - \frac{\sigma_0}{\sigma_c}\right)^{-2} \frac{1}{\sigma_c} H\,(\sigma - \sigma_0).
\end{aligned}
\tag{A1}
$$

Choosing $\sigma_0 = 0$ and substituting σ_c by (12) and (13) yields

$$
m^2(H, \sigma) = m_0^{\,2}\big|_H + \frac{6\lambda_s\mu_0}{J_s^2}(\chi\, m_0)\big|_H \frac{H}{H_A}\sigma. \tag{A2}
$$

Inserting (A2) in (10) yields (without denoting the H-dependence)

$$
\sigma = E_s\left(\frac{\partial u}{\partial x} - \frac{3\lambda_s}{2}\left(m_0^{\,2} + \frac{6\lambda_s\mu_0}{J_s^2}\chi\, m_0\,\frac{H}{H_A}\,\sigma - \frac{1}{3}\right)\right). \tag{A3}
$$

This linear equation in σ can be solved easily

$$
\sigma \approx \frac{E_s}{1 + E_s\,\frac{9\lambda_s^2\mu_0}{J_s^2}\chi\, m_0\,\frac{H}{H_A}}\left(\frac{\partial u}{\partial x} - \frac{3\lambda_s}{2}\left(m_0^{\,2} - \frac{1}{3}\right)\right). \tag{A4}
$$

With the assumed homogeneous material and homogeneous inner field H, the only position-dependent quantity in the above expression is $\frac{\partial u}{\partial x}$. When inserting (A4) in (4), all homogeneous terms can be dropped. Using (7), the equation of motion reads

$$
\rho\,\frac{\partial^2}{\partial t^2}u(x,t) = \frac{E_s}{1 + E_s\,\frac{9\lambda_s^2\mu_0}{J_s^2}\chi\, m_0\,\frac{H}{H_A}}\frac{\partial}{\partial x^2}u(x,t). \tag{A5}
$$

Compared with the equation of motion of a non-magnetostrictive material

$$
\rho\,\frac{\partial^2}{\partial t^2}u(x,t) = E_{\text{eff}}\,\frac{\partial}{\partial x^2}u(x,t). \tag{A6}
$$

One can conclude that the effective Young's modulus for the dynamics of a magnetostrictive material can be calculated in the limits of a first-order approximation regarding σ by

$$
\frac{1}{E_{\text{eff}}} = \frac{1}{E_s} + \frac{9\lambda_s^2\mu_0}{J_s^2}\,\chi\, m_0\,\frac{H}{H_A}. \tag{A7}
$$

This expression for the Delta-E effect is very similar to the expression (2) obtained by Herzer. They would be equal for $\chi\, m_0\,\frac{H}{H_A} = \chi\, m_0^{\,2}$, which is the case for linear or saturated magnetization. For a linear magnetization, both expressions lead to

$$
\frac{1}{E_{\text{eff}}} = \frac{1}{E_s} + \frac{9\lambda_s^2 H^2}{J_s H_A^3}, \tag{A8}
$$

which is exactly the expression for the Delta-E effect obtained by Livingston.[5] The one-dimensional equation of motion (A8) with constant E_{eff} can be solved analytically. When calculating the dynamics of a real magnetostrictive sample, the assumptions made in this section do not apply. In a homogeneous and constant external bias field, the inner magnetic field is generally not homogeneous nor is it constant. The latter is caused by the oscillating stray field, which superposes the constant bias field. To account for both effects, the magnetostatic problem has to be solved simultaneously with the equation of motion.

[1]G. Herzer, J. Magn. Magn. Mater. **254**, 598–602 (2003).
[2]C. A. Grimes, C. S. Mungle, K. Zeng, M. K. Jain, W. R. Dreschel, M. Paulose, and K. G. Ong, Sensors **2**, 294–313 (2002).
[3]C. A. Grimes, S. C. Roy, S. Rani, and Q. Cai, Sensors **11**, 2809 (2011).
[4]C. Liang, S. Morshed, and B. C. Prorok, Appl. Phys. Lett. **90**, 221912 (2007).
[5]J. D. Livingston, Phys. Status Solidi A **70**, 591–596 (1982).
[6]G. Herzer, Z. Metallkd. **93**, 978 (2002).
[7]G. Engdahl and L. Svensson, J. Appl. Phys. **63**, 3924 (1988).
[8]L. Baňas, Math. Models Meth. Appl. Sci. **28**, 1939–1954 (2005).
[9]J. L. Pérez-Aparicio and H. Sosa, Smart Mater. Struct. **13**, 493 (2004).
[10]S. Cao, B. Wang, J. Zheng, W. Huang, Y. Sun, and Q. Yang, IEEE Trans. Magn. **42**, 911 (2006).
[11]O. Bottauscio, M. Chiampi, A. Lovisolo, P. E. Roccato, and M. Zucca, J. Appl. Phys. **103**, 07F121 (2008).
[12]P. G. Evans and M. J. Dapino, IEEE Trans. Magn. **47**, 221 (2011).
[13]S. Chakrabarti and M. J. Dapino, Smart Mater. Struct. **20**, 105034 (2011).
[14]P. G. Evans and M. J. Dapino, J. Appl. Phys. **107**, 063906 (2010).
[15]K. Jin, Y. Kou, and X. Zheng, Smart Mater. Struct. **21**, 045020 (2012).
[16]G. Engdahl, *in Handbook of Giant Magnetostrictive Materials* (Academic Press, San Diego, 2000), pp. 127–205.
[17]R. Becker and W. Döring, *Ferromagnetismus* (Springer, 1939), p. 1.
[18]J. Barandiaran, M. Vazquez, A. Hernando, J. Gonzalez, and G. Rivero, IEEE Trans. Magn. **25**, 3330 (1989).
[19]T. Schrefl, G. Hrkac, S. Bance, D. Suess, O. Ertl, and J. Fidler, in *Handbook of Magnetism and Advanced Magnetic Materials* (John Wiley & Sons, Ltd., 2007).
[20]G. Akoun and J.-P. Yonnet, IEEE Trans. Magn. **20**, 1962 (1984).
[21]R. Engel-Herbert and T. Hesjedal, J. Appl. Phys. **97**, 074504 (2005).
[22]A. C. Hindmarsh, P. N. Brown, K. E. Grant, S. L. Lee, R. Serban, D. E. Shumaker, and C. S. Woodward, ACM Trans. Math. Softw. **31**, 363 (2005).
[23]Registered trademark of Vacuumschmelze GmbH & Co KG.